Modeling and Control of a 4-port Dual Active Half-Bridge Power Converter

Andrea Zilio
Department of Management and Engineering
University of Padova
Vicenza, Italy
andrea.zilio.5@phd.unipd.it

Youssef A. Fahmy
Department of Electrical Engineering
Columbia University
New York City, USA
y.fahmy@columbia.edu

Paolo Mattavelli
Department of Management and Engineering
University of Padova
Vicenza, Italy
paolo.mattavelli@unipd.it

Matthias Preindl
Department of Electrical Engineering
Columbia University
New York City, USA
matthias.preindl@columbia.edu

***Abstract*—The dual active half-bridge (DAHB) converter allows multiple power sources to be interfaced together while maintaining simple control and high efficiency. This paper presents a novel analysis of the DAHB, with a focus on analytical modeling and dc current control. Departing from prior research, a steady-state model is proposed to compute the current waveforms in the transformer and across the four ports of the converter using a superposition of effects approach. Next, a dc current controller is developed to manage the transformer currents and to achieve the desired currents in the four capacitors. The effectiveness of the proposed model and control algorithm is tested using both simulations and experimental data.**

***Index Terms*—Multi-port converters, Dual Active half-bridge Converter, Steady-State Model**

I. Introduction

The adoption of electric vehicles (EVs) is a significant stride in addressing climate change [1]. However, the EV transition faces hurdles, including the establishment of charging infrastructure, advancements in battery technologies, and enhancement of powertrain efficiency. To tackle these challenges, the dual active bridge (DAB) converter emerges as a compelling solution due to its bidirectional nature, isolation capabilities, and application versatility [2], [3]. Moreover, architectures based on the DAB exhibit a high degree of adaptability for transitioning into multi-port converters, facilitated by their capability to accommodate diverse power sources or loads [4], [5].

A variation of the DAB is the dual active half-bridge (DAHB) topology. It is composed of four capacitors paired with just four switches interconnected by a high-frequency transformer. Its design makes it usable in standalone applications and in more complex circuits, including multilevel and multi-port converters [6], [7].

While the conventional DAHB typically features a primary and secondary voltage source, the capacitor split allows for the incorporation of more sources and loads, yielding a multi-port DAHB configuration. Notably, in [8], a hybrid version is proposed, featuring a half-bridge for the primary side (PS) and a full bridge for the secondary side (SS). In the PS, two batteries are connected in parallel with each capacitor, and the converter is employed to balance the energy between them. This is achieved by utilizing a dc bus connected to the full bridge as an energy tank. A similar variant, employing two half-bridges on both the primary and secondary sides, is explored in [9].

The DAHB allows for the adjustment of voltage across each capacitor, thereby providing greater flexibility, as detailed in [6], [10], [11]. Additionally, the ability to maintain distinct voltages across the four capacitors creates a 4-port converter. This configuration is a promising solution for systems requiring dynamic power distribution and high efficiency. Examples are EV chargers, active battery balancing systems, microgrids, and auxiliary power sources. In these applications, it is important to accurately describe the currents circulating in the transformer and in each converter port as a function of operating parameters. Specifically, the ability to control the current in each port is essential for the adoption of multi-port converters.

This paper deviates from previous studies [10]–[12] by presenting a steady-state model for the average currents across the four ports of the converter as well as the currents in the primary and secondary sides of the transformer. Moreover, it identifies just two distinct cases covering all operating conditions, contrasting with prior analyses. In addition to developing the analytical model, the paper explores the design of a dc current controller and introduces a straightforward yet efficient algorithm for managing currents across the four converter ports. The effectiveness of the proposed model and control algorithm to manage the currents in each port are verified using both PLECS simulations and an experimental setup.

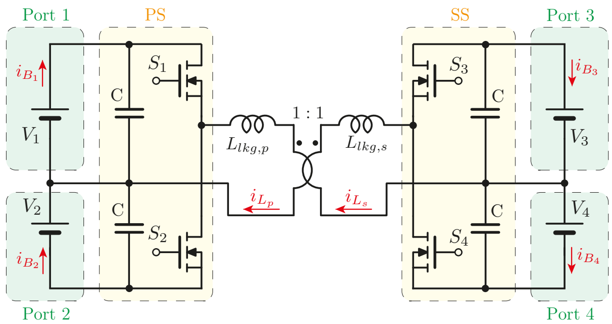

Fig. 1: Schematic of the DAHB.

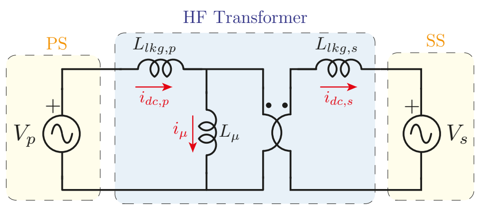

Fig. 2: Equivalent circuit of the high-frequency transformer.

The article is organized as follows. The proposed DAHB topology and its operation are described in Sect. II. In Sect. III, the analytical model is derived. In Sect. IV, the new model is compared with PLECS simulations. A prototype with four bidirectional power sources is used to validate the proposed model and control algorithm in Sect. V. Finally, Sect. VI concludes the article.

II. DAHB Topology

The topology employed in this article is depicted in Fig. 1 where V_i and i_{B_i} are the voltage and current in the i-th port, respectively. It comprises a half-bridge on the PS and a corresponding half-bridge on the SS. The isolation between the primary and secondary sides, as well as the energy transfer, is carried out by a high-frequency transformer equipped with a unity turns ratio; see Fig. 2.

A. Circuit Operation

The proposed DAHB has three operating modes. Mode I is utilized for energy transfer between two ports on the same side. Mode II employs the phase-shift control to allow the bidirectional power flow. Lastly, Mode III integrates both duty cycle and phase-shift to effect power transfer between, for instance, ports 1 and 4 as in Fig. 3.

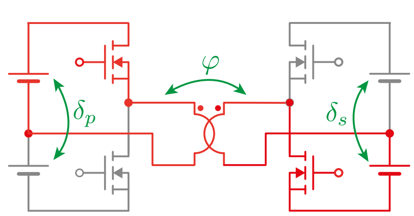

Fig. 3: Operating mode III.

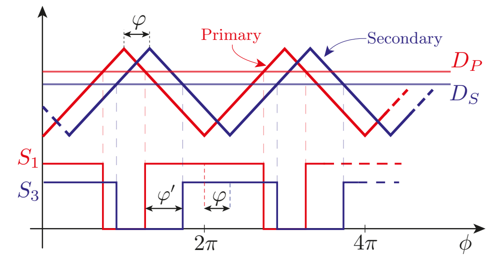

Fig. 4: Carrier signals and switching commands with $\varphi' > 0$.

Given the potential disparity in port voltages, a fixed duty cycle of 50% is unsuitable, as it could lead to transformer core saturation. To mitigate this, it becomes necessary to compute a duty cycle correction factor, thereby ensuring zero voltage imbalance within a switching period T_s. To simplify, it is assumed that the voltage remains constant throughout the switching period. The corrective factor θ_p for the PS is computed as

$$\theta_p = \frac{T_s}{2} \cdot \frac{V_1 - V_2}{V_1 + V_2}. \tag{1}$$

Considering the corrective factor, the steady-state duty cycle for the PS (D_P) and the one for the SS (D_S) are

$$D_P = \frac{V_2}{V_1 + V_2}, \qquad D_S = \frac{V_4}{V_3 + V_4}. \tag{2}$$

As shown in [13], it is possible to regulate the average dc current by merely modulating the duty cycle and therefore exchange energy on the same side of the DAHB.

III. Model Derivation

The analytical model aims to determine the current profiles and average currents across each of the four converter ports based on the phase-shift and the direct currents in both the primary ($I_{DC,p}$) and secondary ($I_{DC,s}$) sides.

The derivation of the analytical model occurs in two steps. Initially, the current profile within the PS is derived, assuming the SS is shorted. This process is then repeated for the SS. In the second step, the currents i_{L_p} and i_{L_s} are determined through the superposition principle.

It is assumed that parasitic elements are negligible and, over T_s, the port voltage is constant and the average leakage inductor current is zero.

In this work, two cases describe all converter operating modes. The boundary condition is expressed as a function of an equivalent phase-shift. It is defined as the distance between the rising edges of the gate-source voltage for S_1 and S_3 denoted with φ' (Fig. 4). It is given by

$$\varphi' = \pi(D_P - D_S) + \varphi. \tag{3}$$

A. Case 1: $\varphi' > 0$

The current on the PS with the SS shorted $i_{L'_p}$ and vice-versa $i_{L'_s}$ are shown in Fig. 5(a). First, the current on the

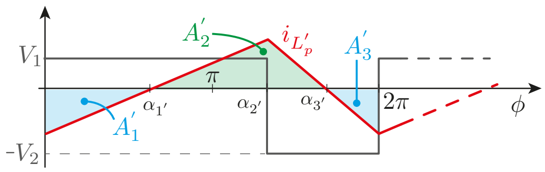

(a) Current on the PS $i_{L_p'}$ with the SS shorted .

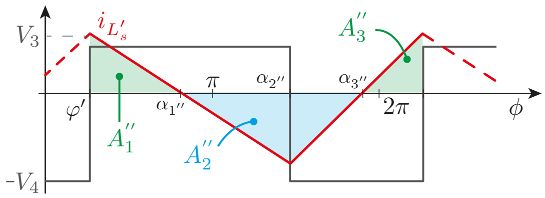

(b) Current on the SS $i_{L_s'}$ with the PS shorted

Fig. 5: Currents across the transformer with $\varphi' > 0$.

PS is derived. The sum of the highlighted areas A_1', A_2', A_3' is set to zero. In the case of $i_{L_p'}$ in Fig. 5(a),

$$A_1' = \tfrac{V_1}{2L_p}\alpha_{1'}^2 \qquad A_2' = \tfrac{V_1}{2L_p}(\alpha_{2'} - \alpha_{1'})(\alpha_{3'} - \alpha_{1'})$$
$$A_3' = \tfrac{V_1}{2L_p}\alpha_{1'}(2\pi - \alpha_{3'}) \tag{4}$$

where $\alpha_{1'}$, $\alpha_{2'}$, and $\alpha_{3'}$ are the zero-crossings, and L_p is the total inductance of the PS. The first term in (5) is derived by imposing that $A_1' + A_3' = A_2'$, the second term by ensuring that the end points of the current waveform are equal, and the third by using the corrective factor θ_p for the PS computed as in (1).

$$\begin{cases} \alpha_{1'}(\alpha_{1'} + 2\pi - \alpha_{3'}) = (\alpha_{2'} - \alpha_{1'})(\alpha_{3'} - \alpha_{1'}) \\ V_1 \cdot \alpha_{1'} = V_2 \cdot (2\pi - \alpha_{3'}) \\ \alpha_{2'} = \pi + \theta_p \end{cases}$$
$$\begin{cases} \alpha_{1'} = \frac{2\pi V_2(\theta_p+\pi)}{V_1(\theta_p+\pi)+V_2(\theta_p+3\pi)} \\ \alpha_{2'} = \pi + \theta_p \\ \alpha_{3'} = \frac{2\pi V_2(\theta_p+3\pi)}{V_1(\theta_p+\pi)+V_2(\theta_p+3\pi)} \end{cases} \tag{5}$$

Accordingly, the current $i_{L_p'}$ in T_s is defined as

$$i_{L_p'}(\phi) = \begin{cases} \frac{V_1}{L_p}(\phi - \alpha_{1'}) & \text{if } \phi < \alpha_{2'} \\ \frac{-V_2}{L_p}(\phi - \alpha_{3'}) & \text{if } \phi \geq \alpha_{2'} \end{cases} \tag{6}$$

Next, the current divider principle is used to find the currents generated by the primary windings in the secondary ($i_{L_{s,p}'}$) and magnetizing ($i_{L_{\mu,p}'}$) windings.

$$\begin{aligned} i_{L_{s,p}'} &= i_{L_p'} \cdot \frac{L_\mu}{L_\mu + L_{lkg,s}} \\ i_{L_{\mu,p}'} &= i_{L_p'} \cdot \frac{L_{lkg,s}}{L_\mu + L_{lkg,s}} \end{aligned} \tag{7}$$

Subsequently, using the same principle as on the PS, the expression for the current in the SS is derived, now considering the PS to be shorted. The $i_{L_s'}$ waveform is shown in Fig. 5(b) and the intersection points are computed as

$$\begin{cases} (\alpha_{1''} - \varphi')(\alpha_{1''} + 2\pi - \alpha_{3''}) = (\alpha_{2''} - \alpha_{1''})(\alpha_{3''} - \alpha_{1''}) \\ V_3 \cdot (\alpha_{1''} - \varphi') = V_4 \cdot (2\pi - \alpha_{3''} + \varphi') \\ \alpha_{2''} = \pi + \theta_s + \varphi' \end{cases}$$
$$\begin{cases} \alpha_{1''} = \frac{V_3\varphi'(\theta_s+\pi)+V_4\varphi'(\theta_s+3\pi)+2\pi V_4(\theta_s+\pi)}{V_3(\theta_s+\pi)+V_4(\theta_s+3\pi)} \\ \alpha_{2''} = \pi + \theta_s + \varphi' \\ \alpha_{3''} = \frac{V_3\varphi'(\theta_s+\pi)+V_4(\varphi'+2\pi)(\theta_s+3\pi)}{V_3(\theta_s+\pi)+V_4(\theta_s+3\pi)} \end{cases} \tag{8}$$

where θ_s is the corrective factor for the SS.

In contrast with (5), the secondary current with the PS shorted is

$$i_{L_s'}(\phi) = \begin{cases} \frac{V_4}{L_s}(\phi + 2\pi - \alpha_{3''}) & \text{if } \phi < \varphi' \\ \frac{-V_3}{L_s}(\phi - \alpha_{1''}) & \text{if } \varphi' \leq \phi < \alpha_{2''} \\ \frac{V_4}{L_s}(\phi - \alpha_{3''}) & \text{if } \phi \geq \alpha_{2''} \end{cases} \tag{9}$$

where L_s is the inductance on the SS. As before, the current divider principle is applied and the primary winding current ($i_{L_{p,s}'}$) and the magnetizing current ($i_{L_{p,\mu}'}$) are

$$\begin{aligned} i_{L_{p,s}'} &= i_{L_s'} \cdot \tfrac{L_\mu}{L_\mu + L_{lkg,p}} \\ i_{L_{\mu,p}'} &= i_{L_s'} \cdot \tfrac{L_{lkg,p}}{L_\mu + L_{lkg,p}} \end{aligned} \tag{10}$$

Finally, using superposition, the current in the PS is

$$i_{L_p} = i_{L_p'} + I_{DC,p} + i_{L_{p,s}'} \tag{11}$$

while, in the SS, the current is

$$i_{L_s} = i_{L_s'} + I_{DC,s} + i_{L_{s,p}'}. \tag{12}$$

At this stage, the currents across the four ports are determined by integrating the current over the periods during which the switches connected in parallel with the ports are conducting. Consequently

$$\begin{aligned} i_{B_1} &= \frac{1}{T_s}\int_0^{\alpha_{2'}} i_{L_p}(\phi)\, d\phi, & i_{B_2} &= -\frac{1}{T_s}\int_{\alpha_{2'}}^{2\pi} i_{L_p}(\phi)\, d\phi \\ i_{B_3} &= \frac{1}{T_s}\int_{\varphi'}^{\alpha_{2''}} i_{L_s}(\phi)\, d\phi, & i_{B_4} &= -\frac{1}{T_s}\int_{\alpha_{2''}}^{2\pi+\varphi'} i_{L_s}(\phi)\, d\phi. \end{aligned} \tag{13}$$

B. *Case 2: $\varphi' < 0$*

The waveforms of the command signals in the case with $\varphi' < 0$ are shown in Fig. 6. Instead, Fig. 7 reports the current waveforms. As can be seen, while having a $\varphi > 0$ the φ' can be negative given its dependence on duty cycle values. As in the case with $\varphi' > 0$, the crossing positions are computed and the same principle illustrated before is applied for calculating $i_{L_p'}$. However, while the most

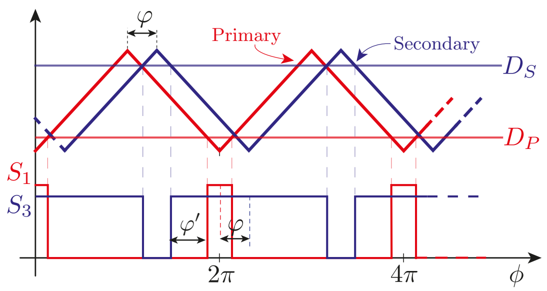

Fig. 6: Carrier signals and switching commands with $\varphi' < 0$.

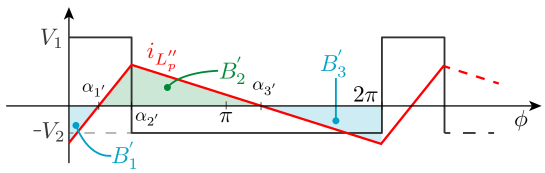

(a) Current on the PS $i_{L_p'}$ with the SS shorted .

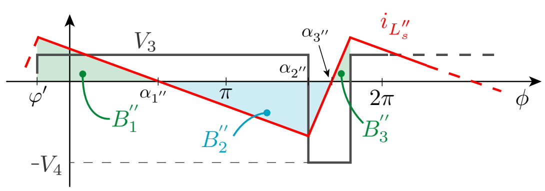

(b) Current on the SS $i_{L_s'}$ with the PS shorted

Fig. 7: Currents across the transformer with $\varphi' < 0$.

part of the equations remain unchanged the current in the secondary has a different structure as shown below

$$i_{L_s''}(\phi) = \begin{cases} \frac{-V_3}{L_s}(\phi - \alpha_{1''}) & \text{if } \phi < \alpha_{2''} \\ \frac{V_4}{L_s}(\phi - \alpha_{3''}) & \text{if } \alpha_{2''} \leq \phi < 2\pi + \varphi' \\ \frac{-V_3}{L_s}(\phi - 2\pi - \alpha_{1''}) & \text{if } \phi \geq 2\pi + \varphi' \end{cases} \tag{14}$$

The expressions for the port currents remain unchanged.

IV. Simulation Comparison

To validate the accuracy of the proposed model, the circuit configuration is realized using PLECS. The converter parameters are $V_{i,NOM} = 200\,\mathrm{V}$, $f_s = 100\,\mathrm{kHz}$, $L_{lkg,p} = L_{lkg,s} = 21.3\,\mu\mathrm{H}$, $L_\mu = 0.24\,\mathrm{mH}$, and $C = 24\,\mu\mathrm{F}$.

The dc current regulation is realized using two PI controllers, for the PS and SS respectively. The reference is the dc current value and the output is the duty cycle. While it holds true that the dc component predominantly hinges on the duty cycle within each branch, this principle does not maintain validity during transient phases. Hence, leveraging the transformer model depicted in Fig. 2, $i_{dc,p}(s)$ can be derived as follows

$$i_{dc,p}(s) = \frac{\delta_1(s)(V_1 + V_2)}{sL_p} - \frac{V_2 + V_s(s) \cdot L_x}{sL_p} \tag{15}$$

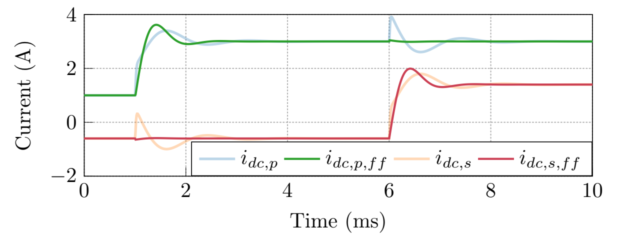

Fig. 8: Dc current control on the PS and SS with and without feed-forward compensation.

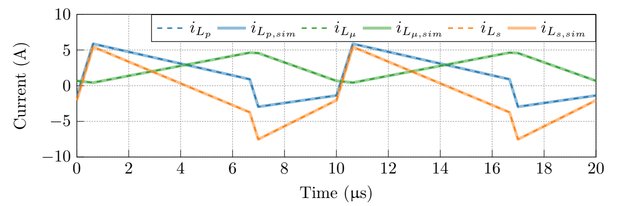

(a) Currents on the transformer

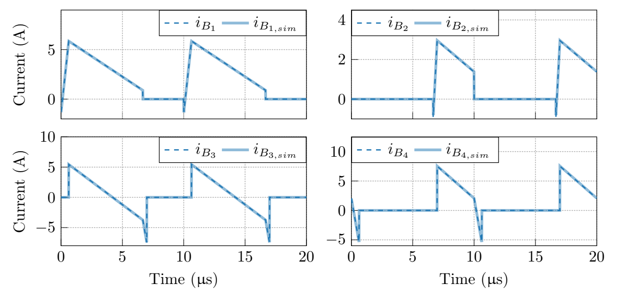

(b) Currents on the 4 ports

Fig. 9: $\varphi' > 0$: $V_{1,2,3,4} = \{150, 300, 200, 350\}\,\mathrm{V}$, $\varphi = 0.3\,\mathrm{rad}$, $I_{DC,P} = 1.5\,\mathrm{A}$, and $I_{DC,S} =$ -1 A.

where $s = j2\pi f_s$, $L_x = L_\mu/(L_\mu + L_{lkg,s})$, and $V_s = \delta_2(V_3 + V_4) - V_4$. It can be seen that $i_{dc,p}$ also depends on the voltage at the secondary. The PI regulator is designed considering only the first term of (15). However, a feed-forward (ff) action can be added to mitigate the effects of the cross-coupling and the results are reported in Fig. 8.

Furthermore, the accuracy of the developed analytical model is verified to determine i_{L_p}, i_{L_μ}, and i_{L_s} in the transformer and i_{B_1}, i_{B_2}, i_{B_3}, and i_{B_4} in each of the four ports. The comparison for the first case ($\varphi' > 0$) in a specific operating point in terms of voltages and dc currents is reported in Fig. 9, while Fig. 10 reports the second case ($\varphi' < 0$). In both scenarios, there is a perfect match between the model and the PLECS simulation.

A. Output Current Control

To control the current in each port, a control scheme is realized consisting of two PI regulators to control the dc current and a third PI that, acting on φ, adjusts the power between the PS and SS.

Starting from the three port references i_{B_1}, i_{B_2}, and i_{B_3}, the dc current reference for the PS is $I_{DC,P} = i_{B_1} -$

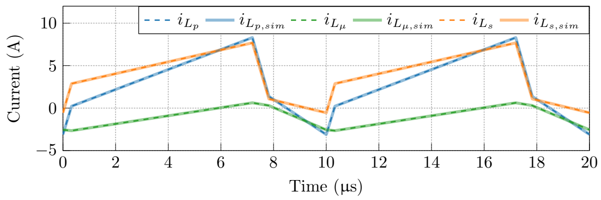

(a) Currents on the transformer

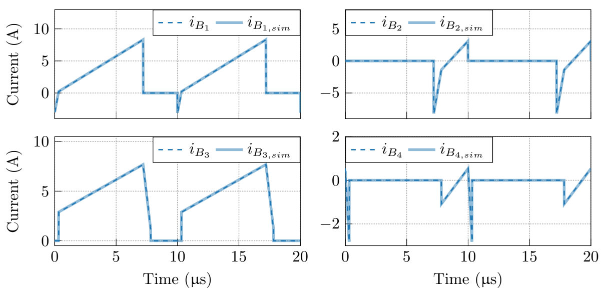

(b) Port currents

Fig. 10: $\varphi' < 0$: $V_{1,2,3,4} = \{140, 360, 100, 300\}$ V, φ = -0.5 rad, $I_{DC,P} = 3$ A, and $I_{DC,S} = 4$ A.

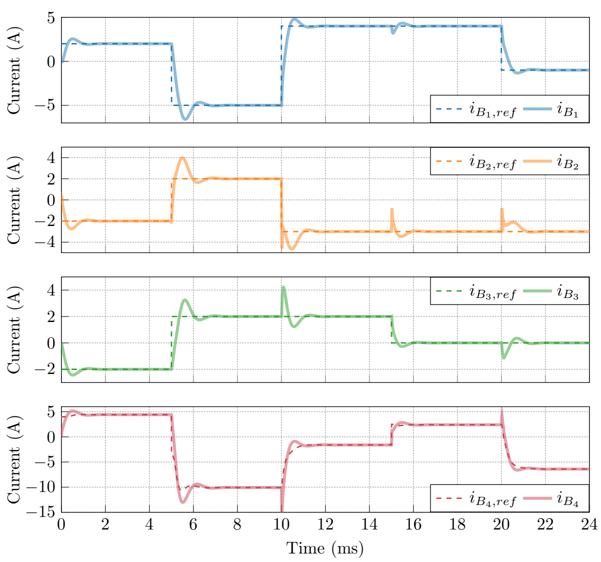

Fig. 11: Performance controlling port currents in PLECS.

i_{B_2} and the primary power is $P_p = V_1 \cdot i_{B_1} + V_2 \cdot i_{B_2}$. Assuming unit efficiency, the secondary power P_s is equal to P_p. Therefore, the power at the 4-th port $P_{i_{B_4}}$ is given by $P_{i_{B_4}} = P_s - V_3 \cdot i_{B_3}$ and $i_{B_4} = P_{i_{B_4}}/V_4$. Finally, the references for the three PI controllers are $I_{DC,P}$, $I_{DC,S} = i_{B_3} - i_{B_4}$, and P_p. The current profiles are shown in Fig. 11.

V. Experimental Setup

The correspondence between the model and experimental data is validated using the prototype shown in Fig.12. The 4-port DAHB prototype is created by configuring a PCB with two half-bridges and four voltage inputs. The MOSFETs used are GeneSiC G3R30MT12K with a

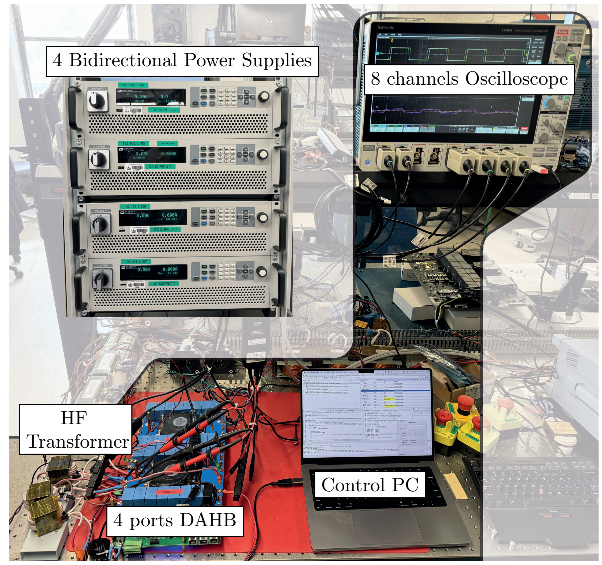

Fig. 12: Experimental Setup.

250ns deadtime. The transformer and external leakage inductors are Ferroxcube 3F36 cores wound with Litz wire, $L_{lkg,p} = L_{lkg,s} = 21.3\,\mu$H, $L_\mu = 0.24$ mH. Each of the ports is connected to an independent bidirectional ITECH power supply to sink and source current.

The analytical model is tested at 4 operating points:

1) *OP1*: $V_{1,2,3,4} = \{100, 100, 100, 100\}$ V, $\varphi = 0$ rad, $\varphi' = 0$ rad, $I_{DC,P} = 0$ A, and $I_{DC,S} = 0$ A;
2) *OP2*: $V_{1,2,3,4} = \{100, 100, 100, 100\}$ V, φ = -0.3 rad, φ' = -0.94 rad, $I_{DC,P} = 1$ A, and $I_{DC,S} = 1$ A;
3) *OP3*: $V_{1,2,3,4} = \{300, 200, 350, 200\}$ V, φ = -0.2 rad, φ' = -0.51 rad, $I_{DC,P} = 1$ A, and $I_{DC,S} = 1$ A;
4) *OP4*: $V_{1,2,3,4} = \{250, 200, 250, 300\}$ V, $\varphi = 0.2$ rad, $\varphi' = 0.31$ rad, $I_{DC,P}$ = -1 A, and $I_{DC,S} = 0$ A;

Tab. I reports the efficiency for each operating point and the percent error between the analytical model and the experimental data. It can be seen that the model estimates the port currents for each operating condition with decreasing error as efficiency increases since losses are not considered in the model derivation.

Next, the accuracy of the model in estimating the transformer currents is verified. The results for *OP3* and *OP4* are shown in Fig. 13(a) and Fig. 13(b), respectively. The analytical model is able to predict current trends with good accuracy at both operating points.

Finally, the control algorithm to achieve the desired output currents is tested in the experimental prototype. An oscilloscope screenshot is shown in Fig. 14. From zero current reference, i_{B_1} and i_{B_2} are raised to 3 and 1.5 A, respectively. The reference is held constant for 240 ms and then changed to 4 and 0.5 A. On the second port, i_{B_3}, is changed from 0 to 3 A for 120 ms and then decreased to 0.5 A for another 120 ms before finishing at 4 A. As designed, all currents settle quickly to their reference values with little overshoot or oscillations.

TABLE I: Comparison between analytical model, PLECS simulations and experimental results.

	$\mathbf{OP_1}$ - $\eta = 71.6\%$				$\mathbf{OP_2}$ - $\eta = 97.9\%$				$\mathbf{OP_3}$ - $\eta = 97.5\%$				$\mathbf{OP_4}$ - $\eta = 97.0\%$			
	i_{B_1}	i_{B_2}	i_{B_3}	i_{B_4}	i_{B_1}	i_{B_2}	i_{B_3}	i_{B_4}	i_{B_1}	i_{B_2}	i_{B_3}	i_{B_4}	i_{B_1}	i_{B_2}	i_{B_3}	i_{B_4}
Mdl	-0.045	0.045	-0.091	0.091	-0.717	-1.640	-0.762	-1.593	-1.797	-2.895	-1.863	-2.461	1.577	3.217	1.598	2.178
Sim.	-0.045	0.045	-0.091	0.091	-0.715	-1.638	-0.763	-1.594	-1.795	-2.893	-1.863	-2.461	1.577	3.218	1.596	2.176
Exp.	-0.021	0.069	-0.124	0.057	-0.656	-1.578	-0.726	-1.557	-1.852	-2.950	-1.918	-2.516	1.560	3.200	1.500	2.080
Err.	53.3	53.3	36.3	37.4	8.51	3.78	4.72	2.26	3.06	1.90	2.95	2.23	1.08	0.53	6.13	4.50

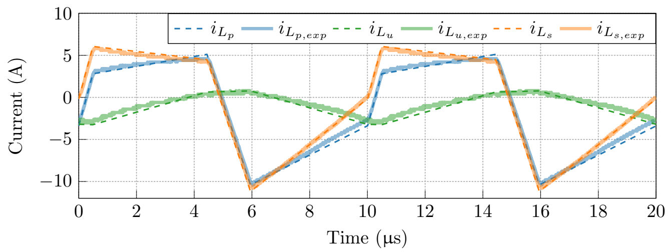

(a) OP_3

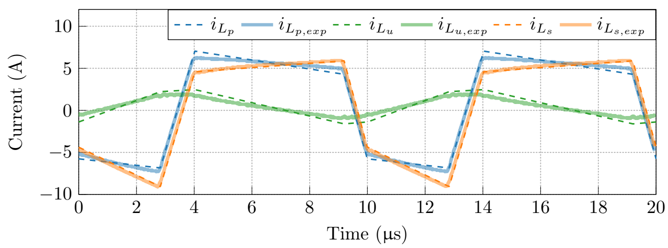

(b) OP_4

Fig. 13: Comparison of analytical and experimental data.

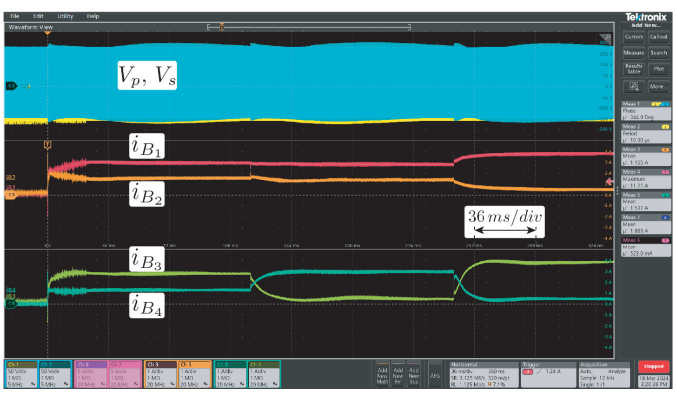

Fig. 14: Performance in controlling port currents using the experimental setup.

VI. Conclusion

This work discusses a novel model and dc current control strategy for the DAHB converter. Through the use of new methodologies, the proposed steady-state model has only two cases making it simpler than those previously discussed in literature. The boundary between the cases is expressed as a function of an equivalent phase-shift and it effectively computes the current waveforms across the transformer and the four ports of the converter using a superposition of effects approach. The effectiveness of both the analytical model and control algorithm has been rigorously evaluated through comprehensive testing involving PLECS simulations and an experimental prototype. Both simulation and experimental results showed that the derived model can determine current profiles and control currents in all four ports under different operating conditions with negligible errors.

References

[1] E. A. Nanaki *et al.*, "Climate change mitigation and deployment of electric vehicles in urban areas," *Renewable energy*, vol. 99, pp. 1153–1160, 2016.

[2] L. Li *et al.*, "Review of Dual Active Bridge Converters with Topological Modifications," *IEEE Transactions on Power Electronics*, 2023.

[3] S. Shao *et al.*, "Modeling and Advanced Control of Dual-Active-Bridge DC–DC Converters: A Review," *IEEE Transactions on Power Electronics*, vol. 37, no. 2, pp. 1524–1547, 2022.

[4] A. A. Ibrahim *et al.*, "Optimal Modulation of Triple Active Bridge Converters by an Artificial-Neural- Network Approach," *IEEE Transactions on Industrial Electronics*, vol. 71, no. 3, pp. 2590–2600, 2024.

[5] ——, "Online Loss Reduction of Isolated Bidirectional DC-DC Quad-Active Bridge Converters," in *2023 IEEE International Transportation Electrification Conference (ITEC)*. IEEE, 2023, pp. 1–6.

[6] Y. A. Fahmy *et al.*, "Switching Permutations and State-Space Modeling of the Dual Active Half Bridge Converter," in *IECON 2022–48th Annual Conference of the IEEE Industrial Electronics Society*. IEEE, 2022, pp. 1–6.

[7] A. Zilio *et al.*, "A Multiport Converter for Flexible Active Balancing in Li-Ion Batteries," *IEEE Transactions on Industrial Electronics*, 2023.

[8] W. Wang *et al.*, "Dual Cell Links for Battery-Balancing Auxiliary Power Modules: A Cost-Effective Increase of Accessible Pack Capacity," *IEEE Transactions on Industry Applications*, vol. 56, no. 2, pp. 1752–1765, 2020.

[9] ——, "A Low-Cost Battery-Balancing Auxiliary Power Module With Dual-Active Half Bridge Links and Coreless Transformers," *IEEE Transactions on Transportation Electrification*, vol. 9, no. 3, pp. 3801–3809, 2023.

[10] F. Gao *et al.*, "Three degrees of freedom operation of a dual half bridge," in *2019 21st European Conference on Power Electronics and Applications (EPE'19)*. IEEE, 2019, pp. P–1.

[11] S. Chakraborty *et al.*, "Fully ZVS, minimum RMS current operation of the dual-active half-bridge converter using closed-loop three-degree-of-freedom control," *IEEE Transactions on Power Electronics*, vol. 33, no. 12, pp. 10 188–10 199, 2018.

[12] F. Gao *et al.*, "Average Modeling of a Dual-Half-Bridge Converter Modulated With Three Degrees of Freedom," *IEEE Transactions on Transportation Electrification*, vol. 7, no. 3, pp. 1016–1030, 2021.

[13] W. Wang *et al.*, "Modeling and control of a dual cell link for battery-balancing auxiliary power modules," in *2018 IEEE Applied Power Electronics Conference and Exposition (APEC)*. IEEE, 2018, pp. 3340–3345.